Chemical Geology 490 (2018) 22–29

Contents lists available at ScienceDirect

Chemical Geology

journal homepage: www.elsevier.com/locate/chemgeo

Secondary fluorescence effects in microbeam analysis and their impacts on geospeedometry and geothermometry

Anastassia Y. Borisova[a,b,*], Nail R. Zagrtdenov[a], Michael J. Toplis[c], John J. Donovan[d], Xavier Llovet[e], Paul D. Asimow[f], Philippe de Parseval[a], Sophie Gouy[a]

[a] Géosciences Environnement Toulouse, Université de Toulouse, UPS OMP- CNRS - IRD, 14 Avenue E. Belin, 31400 Toulouse, France
[b] Geological Department, Lomonosov Moscow State University, Vorobievu Gory, 119899 Moscow, Russia
[c] Institut de Recherche en Astrophysique et Planétologie (IRAP) UPS OMP, CNRS, CNES 14 Avenue E. Belin, 31400 Toulouse, France
[d] University of Oregon, CAMCOR, Eugene, OR, USA
[e] Scientific and Technological Centers, Universitat de Barcelona, Lluís Solé i Sabarís, 1-3, 08028 Barcelona, Spain
[f] Division of Geological and Planetary Sciences 170-25, California Institute of Technology, Pasadena, CA 91125, USA

ARTICLE INFO

Editor: D.B. Dingwell

Keywords:
Secondary fluorescence effects
EMPA
SEM
Microanalysis of Cr, Zr and Ti
Ti-in zircon, Ti-in quartz (TitaniQ)
and Zr-in rutile geothermometers
Mineral saturation, geospeedometry

ABSTRACT

Characteristic and bremsstrahlung X-ray emission during electron-specimen interactions in electron microprobe (EPMA) and scanning electron microscope (SEM) instruments causes secondary fluorescence X-ray effects from adjacent (boundary) phases. This is well-known, yet the impact of such effects in microbeam analysis of natural mineral-hosted inclusions and adjacent to mineral-mineral and mineral-glass boundaries are frequently neglected, especially in geospeedometry and geothermometry applications. To demonstrate the important influence of the secondary fluorescence effect on the measured concentration of elements and its consequences for geochemical applications, we consider the effect of mineral-mineral and mineral-glass boundaries in microanalysis of Cr, Zr and Ti both experimentally, using electron probe measurements on cold-pressed material couples, and computationally, using the software suite "CalcZAF/Standard" and its Graphical User Interface (GUI) for the semi-analytical model FANAL (Llovet et al., 2012). We demonstrate, for example, that apparent Cr contents of the order of ~3000 to 5000 ppm in chromite-hosted glass inclusions at 6 μm from the inclusion boundary can be entirely due to secondary fluorescence in the Cr-rich host phase. Because the spatial gradient in secondary fluorescence-induced X-ray emission superficially resembles a diffusion profile, we emphasize the need to quantitatively correct for such effects in any geospeedometry application involving measurement of diffusion profiles adjacent to grain boundaries with large concentration contrasts. We also provide a scheme for estimating analytical errors related to the secondary fluorescence effect when applying geothermometers such as Ti-in-zircon, Ti-in-quartz (TitaniQ) and Zr-in-rutile. Temperature estimates based on trace Ti, Zr and Cr contents in minerals and glasses affected by secondary fluorescence in nearby phases (e.g., rutile, zircon and chromite) can be severely overestimated, in some cases by hundreds of degrees Celsius.

1. Introduction

Characteristic and bremsstrahlung X-ray emission during electron-specimen interactions in electron microprobe (EPMA) and scanning electron microscope (SEM) instruments has been known to cause secondary fluorescence X-ray effects from adjacent (boundary) phases for decades (Reed and Long, 1963). As the result of the interaction of a beam of electrons with a polished sample surface, characteristic and bremsstrahlung X-rays are emitted in all directions from the electron interaction volume (e.g., Castaing, 1951; Llovet et al., 2012). The primary photons penetrate the specimen and can further ionize atoms at much larger distances than electrons, thereby producing secondary fluorescence and degrading the spatial resolution of the technique and the accuracy of measured concentrations. The contribution from secondary fluorescence in adjacent phases extends tens to hundreds of micrometers from phase boundaries and can cause concentration artifacts up to the weight percent level in some cases. Particularly when measuring trace element concentrations near grain boundaries, it is important to take these effects into consideration during electron microprobe analysis. Of course, secondary fluorescence occurs within homogeneous phases also, but this effect is quantitatively accounted for by all standard matrix correction algorithms; it is only when the target

* Corresponding author at: Géosciences Environnement Toulouse UMR 5563, Observatoire Midi Pyrénées, 14 Avenue E. Belin, 31400 Toulouse, France.
E-mail address: anastassia.borisova@get.omp.eu (A.Y. Borisova).

https://doi.org/10.1016/j.chemgeo.2018.05.010
Received 21 November 2017; Received in revised form 16 March 2018; Accepted 7 May 2018
Available online 09 May 2018
0009-2541/

is inhomogeneous, such as near a phase boundary, that worrisome artifacts are likely to arise (see e.g. Llovet and Galán, 2003; Wade and Wood, 2012). For example, measurements of Cr concentrations in chromite-hosted mineral or glass inclusions with diameters up to tens of μm (Schiano et al., 1997; Spandler et al., 2005; Borisova et al., 2012, Husen et al., 2016) are likely affected by the secondary fluorescence from the chromite host, but this effect has generally been neglected in the literature (e.g., Zhao et al., 2015). Modeling of secondary fluorescence across boundaries between olivine and Ca-containing minerals has been performed by Adams and Bishop (1986) using empirical methods and by Llovet and Galán (2003) using an earlier version of the PENEPMA program. More recently, Goodrich et al. (2014) used the computer code FANAL (Llovet et al., 2012) to correct for secondary fluorescence effects between silicate minerals (olivine and pyroxene) and Cr-rich mineral phases. To our knowledge, no modeling of the effect on Cr analyses of glasses has been published. Although a recent study of chromite saturation in Fe-bearing silicate melts (Zagrtdenov et al., 2018) noted that secondary fluorescence could influence Cr concentration measured by EPMA, they were able to rely on measurements on glass spots at least several hundred μm from the nearest chromite grain, avoiding the need for a quantitative evaluation of boundary effects.

A preliminary calculation of the secondary fluorescence effect on Ti measurements in quartz in contact with TiO_2 was performed by Llovet et al. (2012). The authors estimated that, even when the electron beam impacts SiO_2 at a distance of 100 μm from the TiO_2 phase, the fluorescence contribution yields an apparent Ti concentration of 100 ppm. This is a strong effect that will evidently cause major errors in temperature estimation using the Ti-in-quartz (TitaniQ) thermometer (Wark and Watson, 2006; Ferry and Watson, 2007; Thomas et al., 2015). Thomas et al. (2015) were able to mitigate this effect by performing EPMA measurements of Ti concentrations in areas of quartz grains at least 200 μm away from neighboring rutile and zircon crystals, though of course surface examination only cannot reveal the presence of inclusions buried below the surface. The same effect was explicitly demonstrated for Ti concentrations in quartz adjacent to rutile during the calibration of TitaniQ (Wark and Watson, 2006; Watson et al., 2006). These authors observed that the secondary fluorescence effect generates an apparent concentration of ~300 ppm Ti in quartz 50 μm away from a nearby rutile crystal when analyzed at an accelerating voltage of 15 kV. It has been qualitatively remarked that the secondary fluorescence effect is also severe during measurements of Ti content in zircon coexisting with rutile (or other Ti-rich phases), with potential impact on the Ti-in-zircon thermometer (Ferry and Watson, 2007; Fu et al., 2008), and during analysis of Ti in silicate glasses saturated with rutile (Hayden and Watson, 2007).

The secondary fluorescence effect during zirconium analysis in silicate glasses by EPMA has also sometimes been considered in geochemical studies of chemical diffusion (e.g., Harrison and Watson, 1983) and Zr-based geothermometers (Thomas et al., 2015). For example, Thomas et al. (2015) were able to limit themselves to EPMA measurements of Zr at spots > 200 μm away from neighboring zircon crystals to minimize the secondary fluorescence effect.

Aside from the few studies just mentioned and a few studies of the effect in geological (Adams and Bishop, 1986; Wade and Wood, 2012) and non-geological systems (Bastin et al., 1984; Fournelle et al., 2005), however, there are many instances where the simple solution of limiting analysis to points sufficiently distant from a boundary is not practical or possible or where published work has neglected this effect altogether. The work presented here is intended to demonstrate the important influence of the secondary fluorescence effect on the measured concentration of elements, especially in the cases of natural mineral-hosted inclusions, mineral-mineral and mineral-glass boundaries. We assess the secondary fluorescence boundary effect on measured concentrations of trace elements (Cr, Ti, Zr) for typical analysis conditions of commonly encountered systems of geological relevance. We demonstrate the accuracy and utility of practical theoretical models of the effect by direct comparison with experiments and expand on best practices for avoiding or quantitatively correcting for artifacts in characterization of diffusion profiles and application of minor-element-based geothermometers. More detailed study of the influence of the choice of analytical conditions will be the subject of future work.

2. Materials and methods

2.1. Modeling with FANAL

The freely available software "CalcZAF/Standard" (http://probesoftware.com/download/CalcZAF.msi) contains a GUI to both FANAL and the Monte Carlo simulation program PENEPMA (Llovet and Salvat, 2017). FANAL implements the semi-analytical model of Llovet et al. (2012) for the fast calculation of secondary fluorescence near a planar material boundary perpendicular to the polished surface of a semi-infinite sample. The intensities of primary photons needed for the calculation are obtained from short runs of a modified version of PENEPMA, called PENFLUOR, for both couple materials A and B, and for a homogeneous reference material M (standard). Least-squares fits of the simulated intensities using PENFLUOR give the parameters of the analytical expressions used in the model for each material, which enables FANAL to compute the total K-ratio K(d):

$$K(d) = \frac{I_A + J_{AB}(d)}{I_M + J_M}, \quad (1)$$

where I_A is the primary fluorescence intensity of the considered X-ray line in material A, $J_{AB}(d)$ is the total secondary fluorescence intensity from a A–B couple when the beam impacts on material A at a distance d from the interface, and (I_M) and J_M are the primary and secondary fluorescence intensities, respectively, from homogeneous standard material M, calculated under the same analytical conditions. FANAL assumes that both materials A and B are semi-infinite media separated by a plane interface perpendicular to the surface of the specimen and that the detector is located over material B, thus accounting for absorption of secondary fluorescence only in the fluorescing phase. The modeling results for Cr, Ti and Zr are given in Figs. 1–3.

2.2. Materials and methods

The following six material couples were prepared: synthetic pressed Cr_2O_3 – basaltic glass (mid-ocean ridge basalt, MORB); natural rutile

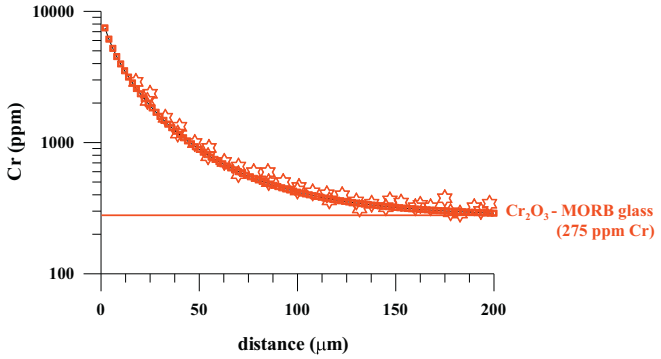

Fig. 1. Comparison of measured (red stars) and calculated (red squares) Cr concentration profiles (in ppm) for a natural Fe-bearing mid-ocean ridge basalt (MORB) glass in contact with synthetic Cr_2O_3. The displayed "background" red line for Cr (bulk-rock) content of 275 ppm in the basaltic glass was taken from Borisova et al. (2018). The modeled concentrations of Cr have been corrected according to the location of the EPMA detector relative to the fluorescing phase of Cr_2O_3 to be comparable to the experimental data. (For interpretation of the references to colour in this figure legend, the reader is referred to the web version of this article.)

(TiO_2) – natural hydrothermal quartz; rutile – rhyolite glass (Macusani obsidian, MAC); rutile – zircon (Mud Tank zircon); zircon – basaltic MORB glass; and zircon – rhyolite glass (Caucasus obsidian). The MORB glass is from the Mid-Atlantic ridge and its composition is given by Borisova et al. (2018). Natural rutile from Mozambique (AMNH27404) was provided by the American Museum of Natural History (New York, USA). Hydrothermal quartz is from the Musée d'Histoire Naturelle (Toulouse, France). Zircon is the Mud Tank zircon (e.g., Yuan et al., 2008). Macusani obsidian glass (MAC) is a well-known homogeneous rhyolite glass frequently used as reference material (Pichavant et al., 1988; Borisova et al., 2010 and references therein) and Caucasus obsidian is a natural rhyolite glass from the Caucasus region from family collection of A.Y. Borisova. Doubly-polished slices of minerals and glasses ~1 mm thick were prepared for cold pressing. Polished surfaces of each mineral-mineral or mineral-glass couple were pressed together under ≤30 kN load and filled with epoxy, then sectioned perpendicular to the interface and re-mounted in epoxy for electron microscope and microprobe studies. Detailed observation of possible mineral inclusions in minerals and glasses were performed at Géosciences Environnement Toulouse (GET, Toulouse, France) using a scanning electron microscope (SEM, JEOL JSM-6360 LV) equipped with an energy dispersive X-ray spectrometer (EDS). The prepared zones have no traces of micrometric inclusions, excluding possible additional effects of secondary fluorescence (i.e., micrometric inclusions of rutile in the hydrothermal quartz) on the experimental measurements. Nevertheless, because most of the starting materials are natural products (glasses and minerals), they may be slightly heterogeneous with respect to Ti and Zr content, giving some "fluctuations" in the apparent trace element concentrations, especially in silicate glasses (Figs. 2, 3).

Major and minor element compositions of the crystals and glasses and determination of apparent concentrations along three to five different profiles across the investigated couple materials were performed using the CAMECA SX-Five microprobe at the Centre de Microcaractérisation Raimond Castaing (Toulouse, France). Operating at 15 kV accelerating voltage, an electron beam of 20 nA (for Ti and Cr) or 100 nA (for Zr) current, < 1 μm in diameter (based on cathodoluminescence), was focused on the sample to give a nominal analytical lateral resolution (i.e., accounting for electron multiple scattering only) of ≤2 μm. Concentration profiles were measured with step sizes ranging from 7 to 15 μm. Synthetic Cr_2O_3 (Cr) and natural albite (Na), corundum (Al), wollastonite (Si, Ca), sanidine (K), pyrophanite (Mn, Ti), hematite (Fe), periclase (Mg), and reference zircon (Zr) standards were used for calibration. Element and background counting times for most analyzed elements were 10 and 5 s, respectively, whereas peak counting times were 120 s for Cr, 110 s for Ti and 240 s for Zr. Detection limits were 70 ppm for Cr and Zr and 120 ppm for Ti. The mafic silicate reference glasses of MPI-DING (KL2-G and ML3B-G of Jochum et al., 2006) were analyzed as unknown samples to monitor the precision and accuracy of the analyses. The reference material analysis demonstrated that precision for the major and minor (e.g., Cr, Ti, Zr in glasses) element analyses is equal to the limit imposed by counting statistics and ranges from 0.5 to 3% (1σ RSD = relative standard deviation), depending on the concentrations of the elements in the reference glasses. Additionally, imaging of the EPMA beam spots along profiles and the measurements of the distance from the couple margin to the beam spots were performed at the GET laboratory using the SEM (JEOL JSM-6360).

3. Results

3.1. Experiments on cold-pressed couple materials

The cold-pressed material couples allow us to investigate the secondary fluorescence effect in a simple geometry matching precisely that assumed in the FANAL models. All experimental data are represented in the Supplementary Dataset. For the case of pure Cr_2O_3 in contact with basaltic glass, Fig. 1 shows that the measured chromium concentration progressively decreases from 3000 ppm at 15–20 μm from the crystal-glass interface to the real level of Cr content in the basaltic glass (275 ppm, Borisova et al., 2018) at 150 μm from the Cr_2O_3 crystal. Similarly, the apparent concentrations of titanium in silicates close to the natural rutile phase are about 3000 ppm in all three rutile-bearing couples (i.e., in quartz, zircon, and Macusani rhyolite glass, Fig. 2). The apparent titanium concentrations reach the real Ti content of 300 ppm in the Macusani glass at 100 μm from the boundary. In the zircon – rutile couple, the apparent zirconium concentration in rutile is 200 ppm at 10 μm from the boundary (Fig. 3). Similarly, in the zircon – MORB couple, the apparent Zr contents are 200 ppm at 10 μm distance from the boundary and progressively approach the true Zr concentration in the MORB glass (94 ppm) with increasing distance. In the zircon – rhyolite glass couple, somewhat sparse data indicate elevated Zr concentrations in the Caucasus obsidian glass close to the zircon, decreasing close to the detection limit of 70 ppm within 20–100 μm.

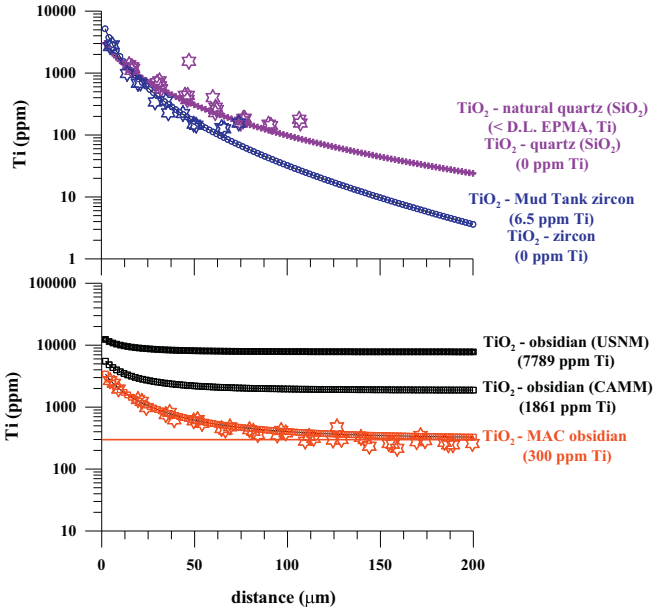

Fig. 2. Upper panel: comparison of measured Ti concentration profiles (in ppm) (stars) in Ti-poor natural quartz and zircon and calculated (crosses and squares) Ti concentration profiles for synthetic Ti-free minerals in contact with rutile (TiO_2). Mud Tank zircon contains 6.5 ± 0.22 ppm Ti (unpublished data of S. Meffre). D.L. EPMA is detection limit (120 ppm of Ti) for the analytical session of EPMA (see Materials and methods section). The modeled concentrations of Ti have been corrected for TiO_2-SiO_2 according to the location of the EPMA detector relative to the fluorescing phase of TiO_2 to be comparable to the experimental data. Lower panel: comparison of measured (red stars) and calculated (red squares) Ti concentration profiles (in ppm) for obsidian glass (MAC) in contact with TiO_2. The displayed "background" red line for Ti (bulk-rock) concentration (300 ppm) in the Macusani (MAC) obsidian was taken from Borisova et al. (2010). Also shown are the calculated Ti concentration profiles for Ti-rich CAMM and USNM obsidian glasses in contact with TiO_2. (For interpretation of the references to colour in this figure legend, the reader is referred to the web version of this article.)

3.2. FANAL calculations

Calculations using the computer code FANAL were performed with configurations matching each of the experimental couples to estimate the effect of secondary fluorescence on apparent concentrations of Cr, Ti and Zr. A correction factor was applied in the cases where the X-ray detector was not located over the fluorescing phase (see above). This correction was obtained from Monte Carlo simulation results with PENEPMA using the actual position of the detector. It amounted to

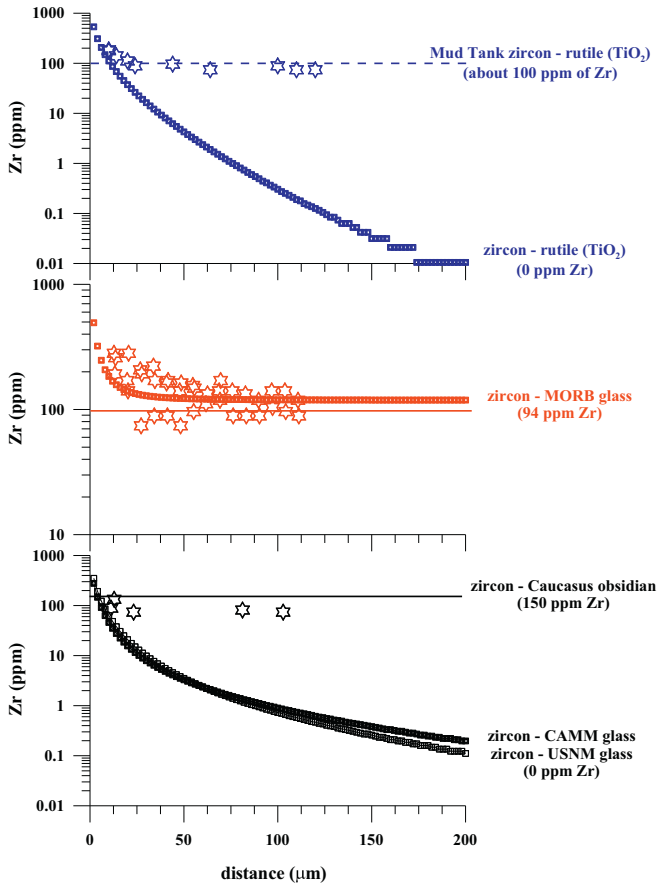

Fig. 3. Upper panel: comparison of measured (stars) Zr concentration profiles for natural rutile (TiO_2) in contact with Mud Tank zircon and calculated (squares) Zr concentration profiles for synthetic Zr-free rutile in contact with synthetic zircon. The displayed "background" Zr concentration in the rutile (~100 ppm), is suggested real concentration in rutile. Middle panel: measured concentration profiles (stars) for MORB glass in contact with Mud Tank zircon and calculated Zr concentration profiles (squares) for the MORB glass (50.3 wt % of SiO_2 content) in contact with a synthetic zircon. The displayed "background" (bulk-rock) Zr concentration of average 94 ppm in the natural MORB glass is from Borisova et al. (2018). Lower panel: measured Zr concentration profiles (stars) for Zr-containing Caucasus obsidian glass (74.7 wt% of SiO_2 content) in contact with Mud Tank zircon. The displayed "background" (bulk-rock) Zr concentrations in the natural Caucasus obsidian glass (average 150 ppm, black line) is unpublished data. Also shown are calculated Zr concentration profiles (squares) for Zr-free obsidian CAMM and USNM obsidian glasses in contact with synthetic zircon. The large scatter in the experimental data is likely due to glass heterogeneity with respect to Zr. The modeled concentrations of Zr have been corrected according to the location of the EPMA detector relative to the fluorescing phase of zircon to be comparable to the experimental data.

3.5% (relative) in apparent Cr concentration for Cr_2O_3-MORB glass (Fig. 1), 9.1% in Ti concentration for TiO_2-SiO_2 (Fig. 2), and for Zr concentration 4.7% in the case of zircon-TiO_2, 23% for zircon-MORB glass and 20.7% for zircon-Caucasus obsidian (Fig. 3). All numerical data are given in the Supplementary Dataset.

It may be seen in Fig. 1 that chromium concentrations of ~3000 ppm and ~5000 ppm in the Fe-bearing basalt are observed at 6 μm distance from boundaries with chromite and Cr_2O_3, respectively. Fig. 1 also demonstrates that the calculated chromium concentrations in the natural MORB basalt near Cr_2O_3 and those of our cold-pressed experiments are the same. Cr concentrations approach the "background" level of Cr content in the basaltic glass at 150 μm distance from the boundary with the Cr_2O_3 phase.

Our modeling of the secondary fluorescence effect for Ti for the obsidian glasses and minerals at the boundary with pure rutile (TiO_2) is illustrated in Fig. 2. A similar level of apparent Ti concentrations (from ~2300 to ~11,000 ppm) at 6 μm distance from the boundary with rutile is seen, depending on the real Ti concentrations in the analyzed materials. In contrast, varying low concentrations of Ti (from 4 to 26 ppm), are observed at 200 μm distance from the boundary in Ti-free zircon and quartz, respectively. The modeled Ti contents in quartz at the boundary with rutile are similar to those previously obtained by Wark and Watson (2006) with a 15 kV incident electron beam. The modeled Ti contents in Ti-free minerals coincide with the measured ones in Ti-poor natural quartz and zircon (above detection limit for Ti), whereas the modeled Ti concentrations in the obsidian glasses (CAMM and USNM) are similar to those measured in natural Macusani (MAC) obsidian glass at ≤ 40 μm distance from the boundary with rutile. Fig. 2 also demonstrates that the calculated Ti concentrations in the natural MAC glass near TiO_2 and those of our cold-pressed experiments are very similar. Ti concentrations approach the "background" level of Ti content in the MAC glass at 100 μm distance from the boundary with the TiO_2 phase boundary.

Similarly, we obtained very similar patterns of secondary fluorescence effects for Zr for both the Zr-free obsidian and the basaltic glasses at the boundary with synthetic zircon, as illustrated in Fig. 3. Apparent Zr concentrations ranging from ~75 to 200 ppm are both observed and computed at 6 μm distance from the boundary with synthetic zircon. Similarly, low concentrations of Zr (~0.1–0.2 ppm) are calculated in the Zr-free glasses at 200 μm from the boundary. The calculated Zr concentrations are lower than those obtained previously by Harrison and Watson (1983) in zircon-obsidian glass pairs. Higher apparent concentrations of ~200 ppm of Zr are observed in natural rutile at the contact with zircon (Fig. 3). The modeled Zr contents in rutile coincides with those measured at 10 to 20 μm distance from boundary with zircon. The apparent Zr concentrations (75–200 ppm) measured in Zr-bearing natural silicate glasses are higher than the values computed in models that assume Zr-free glasses; the difference at > 20 μm distance from the boundary with zircon is related to real zirconium concentrations in the natural glasses. Indeed, Fig. 3 also demonstrates that the calculated Zr concentrations in the natural MORB glass near zircon and those of our cold-pressed experiments are the same. Zr concentrations approach the "background" level of Zr content in the MORB glass at 20 μm distance from the boundary with the zircon.

Overall, the calculated and measured concentrations (Cr, Ti and Zr) in the near-boundary region coincide for all the investigated systems. The differences in the patterns at larger distances (> 20 μm) from the boundary are related to the real metal concentrations in the minerals and glasses. Naturally, the effect of the secondary fluorescence due to nearby metal-rich phases is most obvious in the minerals and glasses with the lowest concentrations of the metals in question. Compared to values observed/calculated in this work for planar geometry, the secondary fluorescence effect associated with spherical (inclusion) geometry will be enhanced if the inclusion being measured has a low concentration in the element in question, or diminished in the opposite case of a metal-poor host mineral being analyzed next to a metal-rich inclusion. For example, simulations of a semi-spherical particle of SiO_2 embedded in TiO_2, when the beam impacts on the particle center, show a 4-fold increase in the secondary fluorescence intensity as compared to that emitted from a SiO_2-TiO_2 couple consisting of two semi-infinite media at a distance from the planar interface equal to the sphere radius.

4. Discussion

4.1. Errors in geothermometers

The documented secondary fluorescence effects translate into potential errors in Zr-in-rutile, Ti-in-zircon, and Ti-in-quartz thermometers that can be far larger than the nominal uncertainties of the respective calibrations, as described here.

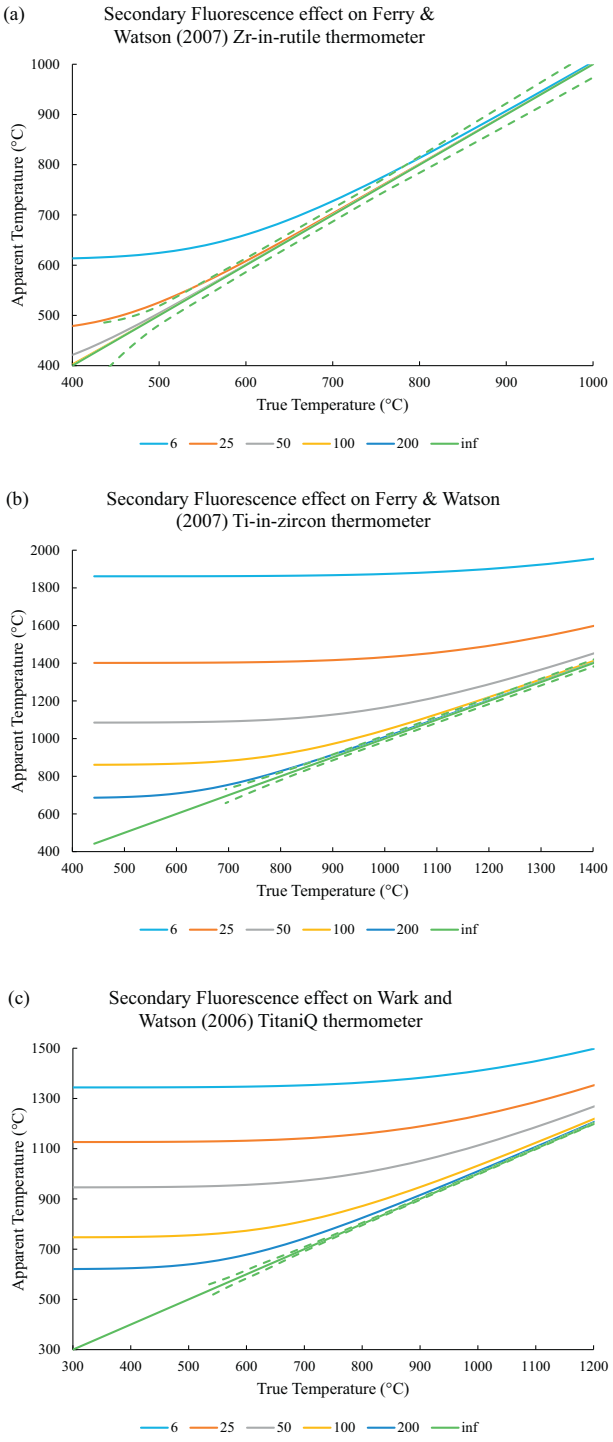

Fig. 4. Visualization of the magnitude of temperature errors due to secondary fluorescence for the (a) Ferry and Watson (2007) Zr-in-rutile thermometer in rutile adjacent to a zircon boundary, (b) the Ferry and Watson (2007) Ti-in-zircon thermometer in zircon adjacent to a rutile boundary, and (c) the Wark and Watson (2006) TitaniQ thermometer in quartz adjacent to a rutile boundary. The real concentrations present are taken from the thermometer calibrations and the apparent concentration used to calculate apparent temperature is the sum of the equilibrium concentration and the apparent counts due to secondary fluorescence. Curves are plotted for analytical points centered at 6, 25, 50, 100, and 200 μm from the boundary. The solid "inf" line is plotted for distance far enough that there is no secondary fluorescence effect and is bounded by dashed lines indicating the 95% confidence interval on each thermometer as given by the original authors, accounting for both systematic error due to the calibration and typical four-spectrometer electron probe errors at the equilibrium concentration values.

Of the three geothermometers considered, Zr-in-rutile appears least subject to secondary fluorescence errors because the effect has the shortest range and the lowest intensity compared to expected equilibrium concentrations, although the small size of natural rutile grains may nevertheless make it difficult to avoid errors. The apparent 200 ppm content of Zr observed in natural Zr-free rutile at a distance of 6 μm from the contact with zircon corresponds to a maximum temperature overestimate of ~200 °C (Fig. 4a) according to the calibrations of Watson et al. (2006) and Ferry and Watson (2007) (N.B., we assume activity of both SiO_2 and TiO_2 equal to 1 here and in the following calculations). Considering the analytical measurement to be exact, the "calibration uncertainty" at this temperature is ~15 °C, and nominal analytical uncertainty on a measurement of 200 ppm Zr by EMPA could yield analytical temperature uncertainty of ± 5 °C. Yet, in the case of a rutile equilibrated with zircon at, for example, 430 °C and hence containing 10 ppm Zr, the additional 200 ppm apparent Zr from secondary fluorescence would give a temperature of 615 °C, in error by 185 °C or 9 times the nominal uncertainty. Fig. 4a presents a plot of apparent temperature based on analysis of a rutile grain at certain distances from the nearest zircon against true temperature, using the Ferry and Watson (2007) calibration and assuming observed Zr counts will be the sum of those due to an equilibrium concentration of Zr and those due to the secondary fluorescence boundary effect as calculated by FANAL. The formal uncertainty bounds due to calibration error and estimated analytical uncertainty for 4-spectrometer EPMA analysis of Zr are taken directly from Ferry and Watson (2007) and shown as dashed lines around the 1:1 line representing infinite distance from a contaminating Zr grain. We predict apparent temperatures exceeding the true temperature by more than the 95% confidence interval at distances below 25 μm and temperatures up to 525 °C. At temperatures up to 750 °C this threshold is exceeded at distances below 6 μm.

Next, considering the ~2900 ppm of Ti in zircon that we observe at a distance of 6 μm from the contact with rutile, this corresponds to apparent temperatures of 1720–1860 °C according to the equations of Watson et al. (2006) and Ferry and Watson (2007) (Fig. 4b). The calibration uncertainty of Ti-in-zircon is < 22 °C at all reported temperatures and the analytical uncertainty on such a large Ti concentration adds < 5 °C to total temperature uncertainty. Yet a zircon containing 100 ppm real Ti concentration, equilibrated with rutile at a true temperature of 994 °C (Watson et al., 2006) or 1020 °C (Ferry and Watson, 2007), would — if measured 6 μm from the nearest rutile — give an apparent temperature due to the 2900 ppm of extra Ti counts from secondary fluorescence that is 740–855 °C too high (depending which calibration is used), an error of at least 25 standard deviations. Even 200 μm from the rutile phase, the FANAL model predicts 4 ppm of apparent Ti from secondary fluorescence. This would be a significant source of error compared to the calibration uncertainty for any zircon equilibrated at a true temperature ≤950 °C, expected to have 70 ppm real Ti. However, zircons in this range would likely be analyzed by ion microprobe in order to keep total uncertainty from becoming dominated by analytical uncertainty. Fig. 4b presents the estimated effect of the secondary fluorescence boundary artifact on Ferry and Watson (2007) temperature estimates using EPMA analyses of Ti in zircons at various distances from the nearest rutile. In this case the apparent temperatures are higher than the true temperature by more than the 95% confidence interval of the method at points within 200 μm at temperatures below ~850 °C, within 100 μm at temperatures below ~1200 °C, and within 50 μm at all temperatures.

In the case of Ti-in-quartz, the magnitude of the artifacts is the most serious among all the thermometers considered, mediated only by the typical ease of finding very large quartz grains that can be analyzed far from interfering boundaries (Fig. 4c). Our Ti measurements in quartz at distances from 6 to 200 μm from the boundary with rutile range from 2300 down to 2 ppm of Ti (Fig. 2). A quartz grain actually containing 20 ppm Ti, corresponding to a true temperature of 585 ± 5 °C according to the calibration of Wark and Watson (2006), would yield

temperatures from 1419 °C at 6 μm from rutile down to 593 °C at 200 μm from rutile. Fig. 4c shows that, even at 200 μm from rutile, the error due to secondary fluorescence is larger at all temperatures than the combined calibration and analytical precision stated by Wark and Watson (2006), and of course the situation becomes rapidly worse as the distance from rutile decreases.

In short, the potential effects of secondary fluorescence on all three minor element thermometers considered (Zr-in-rutile, Ti-in-zircon, Ti-in quartz) are potentially much larger than the nominal uncertainties in temperatures often reported with these techniques, accounting for both errors in calibration and conventional analytical uncertainties. Although the authors of these calibrations (Wark and Watson, 2006; Watson et al., 2006; Ferry and Watson, 2007) explicitly warned users about these effects when their tools are applied using EPMA data, this is often neglected in practice when analyzing natural samples. Furthermore, although our synthetic couples allow us to control the geometry and find analytical points far enough from the boundary to essentially eliminate the issue, this is not always possible in the analysis of either experimental or natural samples. Rutile and zircon are accessory phases in rocks and their grain sizes are generally quite small. Even quartz, though it can grow to large size, might be zoned and a user might choose to analyze near the rim (and so, potentially, near contamination from a rutile grain) in order to target temperature at a particular stage of mineral growth. Any EPMA measurements of trace Ti concentrations in zircon or quartz, or of trace Zr in rutile, that are near or potentially near (at depth within the sample as well as horizontally on the polished surface) a contact with a Ti- or Zr-rich phase are suspect. Such measurements cannot be used for geothermometry unless the metal concentrations are corrected for the secondary fluorescence boundary effect using a tool such as FANAL.

4.2. Errors in mineral saturation of melts and in metal concentrations of inclusions

Rutile saturation temperatures and TiO_2 activity estimates based on EPMA analyses of Ti in glass are subject to similar errors due to secondary fluorescence if there are rutile grains near the analysis spot. We can quantify the magnitude of potential errors in such calculations using published studies of the Ti concentration in melts at rutile saturation as a function of temperature and melt composition. Hayden and Watson (2007) used EPMA data to build their calibration but avoided any analyses within 150 μm of the large rutile grain at one end of their capsules. Kularatne and Audétat (2014) relied on laser ablation inductively coupled mass spectrometry (LA-ICP-MS), which is not subject to secondary fluorescence errors, and designed their experiments so that laser spots contaminated with rutile grains could be clearly distinguished. Despite the care taken during these studies, application of these calibrations to estimate temperature using EPMA data must also be limited to conditions where secondary fluorescence artifacts are unimportant. For example, we caution that 2500–4400 ppm of excess apparent Ti content will be observed in silicic glasses at a distance of 6 μm from rutile, decreasing to ~100 ppm excess Ti at 100 μm from rutile. Fig. 5 shows the apparent rutile saturation temperatures that would be extracted from these results in Macusani rhyolite glass as a function of true temperature and distance from rutile, according to the model of Hayden and Watson (2007). With the stated parameter uncertainties of the fit (ignoring correlation between parameter uncertainties, which are not given), the excess temperature due to secondary fluorescence is larger than the formal uncertainty of the calibration (20–30 °C) at 50 μm for all temperatures below 775 °C, at 25 μm for all temperatures below 875 °C, and at 6 μm for all temperatures within the calibration range of the thermometer. We cannot apply this analysis to the Kularatne and Audétat (2014) calibration because no information is given on the uncertainty of its saturation temperature estimates, but for Macusani composition the nominal values of the two thermometers are nearly identical. We see again that any measurement

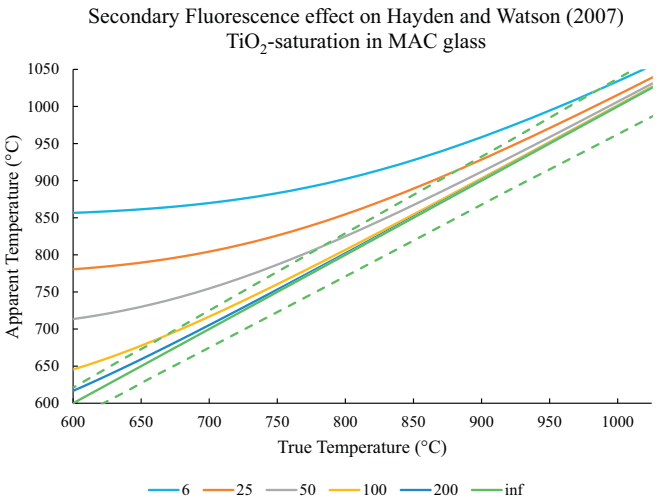

Fig. 5. Visualization of the magnitude of temperature errors due to secondary fluorescence for the Hayden and Watson (2007) Ti-saturation temperature estimate in Macusani obsidian. The format is the same as Fig. 4.

of Ti content in glasses in proximity to rutile by electron microprobe must be corrected using a tool such as FANAL or replaced by alternative micro-analytical methods such as secondary ion mass spectrometry or LA-ICP-MS before it can be applied to rutile saturation thermometry.

Similarly, Fig. 6 shows the apparent chromite saturation temperatures that would be calculated from typical mafic and ultramafic glasses as a function of true temperature and distance from chromite, according to the model of Zagrtdenov et al. (2018). The maximal excess temperature due to secondary fluorescence reaches ~580 °C at 6 μm distance from chromite and the excess temperature is much larger than the formal uncertainty of the calibration (~10 °C) at 50 μm distance for all temperatures below 1350 °C. This effect of secondary fluorescence is especially important for Cr contents in chrome spinel-hosted glass inclusions. For example, Husen et al. (2016) recorded chromite-hosted melt inclusions with up to 11,000 ppm of Cr. The Cr concentrations are much higher than those of mafic melt saturation with chromite at

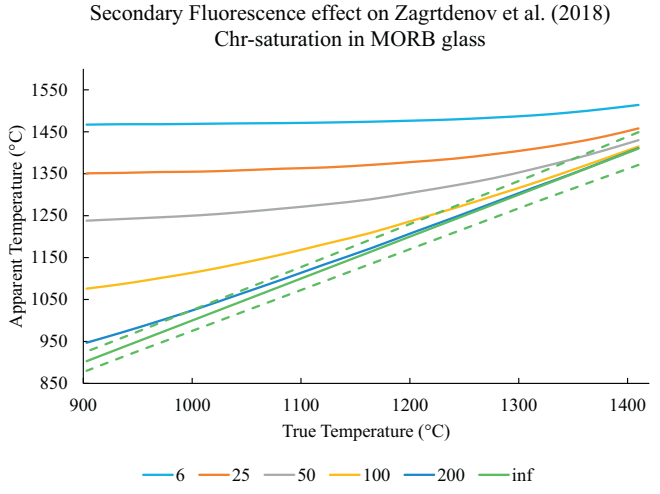

Fig. 6. Visualization of the magnitude of temperature errors due to secondary fluorescence for the Zagrtdenov et al. (2018) chromite (Chr)-saturation temperature estimate in a typical mid-ocean ridge basalt (MORB) glass. The calculated value of λ (optical basicity of the MORB glass) is 0.588 and the applied constant oxygen fugacity (f_{O2}) corresponds to quartz-fayalite-magnetite at 1300 °C. Apparent Cr concentration expressed as X_{Cr}^{liq} (molar fraction of chromium in the silicate glass or liquid) is calculated according to the secondary fluorescence effect. The format is the same as Figs. 4 and 5.

1400–1440 °C and oxygen fugacity corresponding to quartz-fayalite-magnetite mineral buffer (~2800–4500 ppm, depending on the melt composition e.g., Zagrtdenov et al., 2018); certainly any observation of Cr concentrations above 4500 ppm in such natural melt inclusions is contaminated by analytical errors, and lower apparent concentrations may be affected as well.

4.3. Erroneous diffusion profiles

Although the functional form of the decay in boundary-induced secondary fluorescence with distance from an interface is not formally an error function, the curves shown in Figs. 1-3 quantitatively resemble diffusion profiles (at least in linear-linear concentration-distance space; in log-linear space the error function is concave down and the secondary fluorescence decay is concave up). Hence there is some risk that measurements of homogeneous phases near boundaries may be mistaken for diffusion profiles and subsequently interpreted as constraints on diffusivity (in experiments at known time and temperature) or on time-temperature histories (in natural cases). For example, Elardo et al. (2012) show a boundary layer of apparent Cr-enrichment in olivine adjacent to chromite, up to 2700 ppm enrichment and about 60 μm wide. While they acknowledge the possibility that this is a secondary fluorescence effect, they discount this and proceed to interpret the result as a diffusion profile. Given the similarity between composition and mass absorption coefficients in MORB and in olivine, the present results demonstrate conclusively that the profile observed by Elardo et al. (2012) is in fact dominated by a secondary fluorescence boundary effect and not Cr diffusion into olivine. At the very least, the secondary fluorescence profile that is certainly present in the analyses should have been subtracted before attempting to interpret any residual Cr signal as a diffusion profile.

As we show in the case of Cr in MORB glass, the characteristic decay length of the secondary fluorescence effect is about 100 μm. The diffusivity of Cr in a dry phonolite liquid, reasonably similar in viscosity and liquidus temperature to MORB, has been measured by Behrens and Hahn (2009) and, at 1200 °C (a typical dry MORB liquidus temperature), is $\sim 10^{-12}$ m^2/s. It follows by simple scaling analysis that a diffusion profile in chromite-undersaturated MORB liquid around a chromite grain will develop a length comparable to the secondary fluorescence profile length in $\sim 10^4$ s. Likewise, for Cr diffusion in olivine, Ito and Ganguly (2006) report anisotropic diffusivity which, extrapolating to 1200 °C, corresponds to 1.6×10^{-18} m^2/s in the *a* direction and 5.6×10^{-18} m^2/s in the *c* direction. Hence, for olivine in contact with chromite, a diffusion profile similar in length to the secondary fluorescence profile will develop in ~200 years along *a* and ~50 years along *c*. In each case, diffusion operating over timescales much longer than these scaling-estimated times should be readily distinguished from secondary fluorescence. Diffusion over timescales much shorter than these times will be strongly contaminated by secondary fluorescence. However, this does not mean that short diffusion profiles cannot be observed. There are several key differences between diffusion and secondary fluorescence that should allow extraction of real diffusion information. First, we show that CalcZAF/Standard provides a reliable and accurate tool to subtract the secondary fluorescence effect. Second, the boundary concentration in MORB due to secondary fluorescence will always be ~3000–5000 ppm, whereas the boundary condition for diffusion should be controlled by equilibrium partitioning and will vary as a function of pressure, temperature, oxidation state and other variables. In the case of olivine, diffusion if measured in more than one direction or mapped on a plane will display clear anisotropy whereas secondary fluorescence will be isotropic, provided possible directional effects such as X-ray absorption in adjacent phases (see above) and/or Bragg defocusing (Dalton and Lane, 1996) are accounted for. Finally, as emphasized above, in log-linear space the shapes of diffusion and secondary fluorescence profiles are clearly distinct and this can be used to confirm correct subtraction of the secondary fluorescence effect.

5. Conclusions

1) We demonstrate that the computer code FANAL, implemented in the free software CalcZAF/Standard, reproduces accurately the results of Ti, Zr, and Cr analysis profiles in bimaterial couples. In cases where analysis close to a boundary is unavoidable, the model can be used to correct for secondary fluorescence boundary effects.
2) Without correction, geo-thermometric estimates based on electron microprobe measurement of trace Ti and Zr contents in minerals (e.g., quartz, rutile and zircon) and saturation temperatures based on Ti and Cr in glasses can be grossly in error, by far more than the formal uncertainty of the thermometer calibrations, when affected by secondary fluorescence from nearby phases rich in the element in question. We provide a graphical solution to estimate the magnitude of the error as a function of distance and real equilibration temperature. The strongest effect of secondary fluorescence due to a nearby metal-rich phase is found in mineral and glasses with the lowest concentrations of those metals, for example in glass inclusions within metal-rich mineral hosts. Use of alternative micro-analytical methods such as secondary ion mass spectrometry and laser ablation inductively coupled mass spectrometry may be necessary to avoid errors in samples of this type.
3) Diffusion profiles with lengths comparable to 100 μm can be strongly compromised by secondary fluorescence effects. It is important to avoid naïve interpretation of boundary artifacts as diffusion profiles and to correct the observed diffusion profiles using tools such as the CalcZAF/Standard Graphical User Interface for FANAL.

Acknowledgements

A.Y.B. thanks Nadezhda Sushchevskaya, Michel Pichavant, Didier Beziat, Jim Webster, and Sebastian Meffre for providing glass and mineral samples. A.Y.B. thanks Sebastian Meffre for providing unpublished data on reference zircons (e.g., Mud Tank zircon). This work has been supported by ISIFoR (ADERA 450710) grant to A.Y.B. in 2017–2018.

Appendix A. Supplementary data

Supplementary data to this article can be found online at https://doi.org/10.1016/j.chemgeo.2018.05.010.

References

Adams, G.E., Bishop, F.C., 1986. The olivine-clinopyroxene geobarometer: experimental results in the CaO-FeO-MgO-SiO, system. Contrib. Mineral. Petrol. 94, 230–237.
Bastin, G.F., van Loo, F.J.J., Vosters, P.J.C., Vrolijk, J.W.G.A., 1984. An iterative procedure for the correction of secondary fluorescence near phase boundaries. Spectrochim. Acta 39B, 1517–1522.
Behrens, H., Hahn, M., 2009. Trace element diffusion and viscous flow in potassium-rich trachytic and phonolitic melts. Chem. Geol. 259, 63–77.
Borisova, A.Y., Pokrovski, G.S., Pichavant, M., Freydier, R., Candaudap, F., 2010. Arsenic enrichment in hydrous peraluminous melts: insights from LA-ICPMS and in situ X-ray absorption spectroscopy. Am. Mineral. 95, 1095–1104.
Borisova, A.Y., Ceuleneer, G., Arai, S., Kamenetsky, V., Béjina, F., Polvé, M., de Parseval, Ph., Aigouy, T., Pokrovski, G.S., 2012. A new view on the petrogenesis of the Oman ophiolite chromitites from microanalyses of chromite-hosted inclusions. J. Petrol. 53 (12), 2411–2440. http://dx.doi.org/10.1093/petrology/egs054.
Borisova, A.Y., Zagrtdenov, N., Toplis, M.J., Bohrson, W.A., Nédélec, A., Safonov, O.G., Pokrovski, G.S., Ceuleneer, G., Melnik, O.E., Bychkov, A.Y., Gurenko, A.A., Shcheka, S., Terehin, A., Polukeev, V.M., Varlamov, D.A., Chariteiro, K.E.A., Gouy, S., de Parseval, P., 2018. Shallow felsic crust formation on early Earth. Nature Geosci. (under consideration).
Castaing, R., 1951. Application of Electron Probes to Local Chemical and Crystallographic Analysis. PhD thesis, University of Paris. Translated by P. Duwez and D.B. Wittry, California Institute of Technology, Pasadena, California, USA, 1955.
Dalton, J.A., Lane, S.J., 1996. Electron microprobe analysis of Ca in olivine close to grain boundaries: the problem of secondary fluorescence. Am. Mineral. 81, 194–201.
Elardo, S.M., McCubbin, F.M., Shearer Jr., C.K., 2012. The origin of chromite symplectites in lunar troctolite 76535: A new look at an old rock. In: 43rd Lunar and Planetary Science Conference, pp. 1028.

Ferry, J.M., Watson, E.B., 2007. New thermodynamic models and revised calibrations for the Ti-in-zircon and Zr-in-rutile thermometers. Contrib. Mineral. Petrol. 154, 429–437.

Fournelle, J.H., Kim, S., Perepezko, J.H., 2005. Monte Carlo simulation of Nb Kα secondary fluorescence in EPMA: comparison of PENELOPE simulations with experimental results. Surf. Interface Anal. 37, 1012–1016.

Fu, B., Page, F.Z., Cavosie, A.J., Fournelle, J., Kita, N.T., Lackey, J.S., Wilde, S.A., Valley, J.W., 2008. Ti-in-zircon thermometry: applications and limitations. Contrib. Mineral. Petrol. 156, 197–215.

Goodrich, C.A., Harlow, G.E., Van Orman, J.A., Sutton, S.R., Jercinovic, M.J., Mikouchi, T., 2014. Petrology of chromite in ureilites: deconvolution of primary oxidation states and secondary reduction processes. Geochim. Cosmochim. Acta 135, 126–129.

Harrison, T.M., Watson, E.B., 1983. Kinetics of zircon dissolution and zirconium diffusion in granitic melts of variable water content. Contrib. Mineral. Petrol. 84, 66–72.

Hayden, L.A., Watson, E.B., 2007. Rutile saturation in hydrous siliceous melts and its bearing on Ti-thermometry of quartz and zircon. Earth Planet. Sci. Lett. 258, 561–568.

Husen, A., Kamenetsky, V.S., Everard, J.L., Kamenetsky, M.B., 2016. Transition from ultra-enriched to ultra-depleted primary MORB melts in a single volcanic suite (Macquarie Island, SW Pacific): implications for mantle source, melting process and plumbing system. Geochim. Cosmochim. Acta 185, 112–128. http://dx.doi.org/10.1016/j.gca.2016.02.031.

Ito, M., Ganguly, J., 2006. Diffusion kinetics of Cr in olivine and ^{53}Mn-^{53}Cr thermochronology of early solar system objects. Geochim. Cosmochim. Acta 70, 799–809.

Jochum, K.P., Stoll, B., Herwig, K., Willbold, M., Hofmann, A.W., Amini, M., Aarburg, S., Abouchami, W., Hellebrand, E., Mocek, B., Raczek, I., Stracke, A., Alard, O., Bouman, C., Becker, S., Dücking, M., Brätz, H., Klemd, R., de Bruin, D., Canil, D., Cornell, D., de Hoog, C.-J., Dalpé, C., Danyushevsky, L., Eisenhauer, A., Gao, Y., Snow, J.E., Groschopf, N., Günther, D., Latkoczy, C., Guillong, M., Hauri, E.H., Höfer, H.E., Lahaye, Y., Horz, K., Jacob, D.E., Kasemann, S.A., Kent, A.J.R., Ludwig, T., Zack, T., Mason, P.R.D., Meixner, A., Rosner, M., Misawa, K., Nash, B.P., Pfänder, J., Premo, W.R., Sun, W.D., Tiepolo, M., Vannucci, R., Vennemann, T., Wayne, D., Woodhead, J.D., 2006. MPI-DING reference glasses for in situ microanalysis: New reference values for element concentrations and isotope ratios. Geochem. Geophys. Geosyst. http://dx.doi.org/10.1029/2005GC001060. 7/2.

Kularatne, K., Audétat, A., 2014. Rutile solubility in hydrous rhyolite melts at 750 – 900°C and 2 kbar, with application to titanium-in quartz (TitaniQ) thermoberometry. Geochim. Cosmochim. Acta 125, 196–209.

Llovet, X., Galán, G., 2003. Correction of secondary X-ray fluorescence near grain boundaries in electron microprobe analysis: application to thermobarometry of spinel lherzolites. Am. Mineral. 88, 121–130.

Llovet, X., Salvat, F., 2017. PENEPMA: a Monte Carlo program for the simulation of X-ray emission in Electron probe microanalysis. Microsc. Microanal. 23, 634–646.

Llovet, X., Pinard, P.T., Donovan, J.J., Salvat, F., 2012. Secondary fluorescence in electron probe microanalysis of material couples. J. Phys. D. Appl. Phys. 45, 225301 (12 pp.).

Pichavant, M., Kontak, D.J., Herrera, J.V., Clark, A.H., 1988. The Miocene-Pliosene Macusani volcanics, SE Peru. II. Geochemistry and origin of a felsic peraluminous magma. Contrib. Mineral. Petrol. 100, 325–338.

Reed, S.J.B., Long, J.V.P., 1963. Electron probe measurements near phase boundaries. In: Patee, H.H. (Ed.), X-ray Optics and X-ray Microanalysis. Academic, New York, pp. 317–327.

Schiano, P., Clocchiatti, R., Lorand, J.-P., Massare, D., Deloule, E., Chaussidon, M., 1997. Primitive basaltic melt included in podiform chromites from the Oman ophiolite. Earth Planet. Sci. Lett. 146, 489–497.

Spandler, C., Mavrogenes, J., Arculus, R., 2005. Origin of chromitites in layered intrusions: evidence from chromite-hosted melt inclusions from the Stillwater complex. Geology 33, 893–896.

Thomas, J.B., Watson, E.B., Spear, F.S., Wark, D.A., 2015. TitaniQ recrystallized: experimental confirmation of the original Ti-in-quartz calibration. Contrib. Mineral. Petrol. 169, 27.

Wade, J., Wood, B.J., 2012. Metal-silicate partitioning experiments in the diamond anvil cell: a comment on potential analytical errors. Phys. Earth Planet. Inter. 192–193, 54–58.

Wark, D.A., Watson, E.B., 2006. TitaniQ: a titanium-in-quartz gethermometer. Contrib. Mineral. Petrol. 152, 743–754.

Watson, E.B., Wark, D.A., Thomas, J.B., 2006. Crystallization thermometers for zircon and rutile. Contrib. Mineral. Petrol. 151, 413–433.

Yuan, H.-L., Gao, S., Dai, M.-N., Zong, C.-L., Günther, D., Fontaine, G.H., Liu, X.-M., Diwu, C., 2008. Simultaneous determinations of U–Pb age, Hf isotopes and trace element compositions of zircon by excimer laser-ablation quadrupole and multiple-collector ICP-MS. Chem. Geol. 247, 100–118.

Zagrtdenov, N.R., Toplis, M.J., Borisova, A.Y., Guignard, J., 2018. New model of chromite and magnesiochromite solubility in silicate melts. Geochim. Cosmochim. Acta (under revision).

Zhao, D., Zhang, Y., Essene, E.J., 2015. Electron probe microanalysis and microscopy: principles and applications in characterization of mineral inclusions in chromite from diamond deposit. Ore Geol. Rev. 65, 733–748.